Performance evaluation, readout modes and calibration techniques of HgCdTe HAWAII-2RG mosaic arrays

Gert Finger[a*], Reinhold J. Dorn[a], Siegfried Eschbaumer[a], Donald N. B. Hall[b],Leander Mehrgan[a], Manfred Meyer[a] and Jörg Stegmeier[a].
[a]European Southern Observatory, Karl Schwarzschildstrasse 2, D-85748-Garching, Germany.
[b]Institute for Astronomy, University of Hawaii, 640 N Ao`hoku Pl, Hilo HI, 96720, USA.

ABSTRACT

Recently ESO has commissioned the HAWK-I camera which is equipped with a 2x2 mosaic of λ_c~ 2.5 μm HAWAII-2RG arrays. The arrays have high quantum efficiency and achieve photon shot noise limited performance on the telescope. Using reference pixels it can be shown that the readout noise for most arrays is limited by the MBE grown HgCdTe material and not by the multiplexer or the data acquisition chain. Results obtained with the guide window of the HAWAII-2RG multiplexer will be presented. Inter-channel crosstalk and fringing in the detector substrate will be discussed. The dynamic range of detectors can be expanded by applying threshold limited integration (TLI) to the follow-up-the-ramp nondestructive sampling scheme. For substrate removed arrays a calibration technique based on the X-ray emission of Fe^{55} will be discussed.

Keywords: HgCdTe, readout noise, threshold limited integration, guide mode, HAWAII-2RG, MBE, conversion gain, Fe55.

1. INTRODUCTION

Several of the first and second generation near infrared VLT instruments at ESO are equipped with 2Kx2K λ_c~ 2.5 μm HgCdTe HAWAII-2RG arrays, which deliver excellent performance [1]. The integral field spectrograph SINFONI received the first array followed by the HAWK-I camera with a 2x2 mosaic of four arrays mounted on a GL-Scientific mosaic mount [2]. At present, the infrared arm of the X-Shooter cross-dispersed echelle spectrograph which is completing the AIT phase in Europe is equipped with a HAWAII-2RG array [3]. The multi-object spectrograph KMOS will house three of those arrays and the planet finder SPHERE two arrays. Each of the instruments has specific requirements. Readout techniques that have been developed to meet these requirements by making use of the versatile high performance HAWAII-2RG multiplexer will be discussed. The substrate removed arrays arrived just in time to eliminate a severe fringing problem encountered in the X-Shooter spectrograph. With substrate removed arrays it is for the first time also possible to extend the standard Fe^{55} method of calibrating the conversion gain from optical detectors based on Silicon (CCD's) to narrow band-gap infrared detectors.

2. BASIC PARAMETERS: QUANTUM EFFICIENCY AND DARK CURRENT

As shown in the left plot of Figure 1 the HAWAII-2RG arrays have high quantum efficiency exceeding 85% over their entire sensitive wavelength range from λ=0.85 μm, where the CdZnTe substrate cuts off, up to the cutoff wavelength at λ_c~ 2.5 μm. The wavelength dependence of the quantum efficiency was measured with a grating monochromator. The wavelength dependence of the monochromator efficiency was calibrated with a pyroelectric detector which is assumed to have constant spectral response over the entire spectral range. The exit slit of the monochromator is then imaged onto the infrared array. The spectral transmission of all elements in the optical path such as order sorting filters, lenses, windows and cold bandpass filters must be known to derive the spectral quantum efficiency. The monochromator measurement delivers only the relative spectral QE which is converted into an absolute QE by matching the spectral quantum efficiency to a broad band measurement in H with known radiometric geometry. This measurement relies on the emission of a blackbody (SR20 from CI) which was calibrated with a high precision HEITRONIC radiometer calibrated at PTB (German equivalent to NIST). Discrepancies of up to 6 degrees of the displayed and radiometrically measured blackbody temperature were observed.

*gfinger@eso.org; phone +49-89-32006256; fax +49-89-3202362; www.eso.org/~gfinger

The temperature dependence of the dark current of the Hawk-I detectors is shown in the right plot of Figure 1. At temperatures below 80 K most detectors have dark currents below 1E-2 e/s/pixel. The dark current of λ_c~ 2.5 µm arrays is dominated by surface generation-recombination Shockley-Hall-Read processes which are proportional to exp(-E_{gap}/nKT). The parameter n given in the plot was obtained by fitting the exponential temperature dependence of the dark current exp(-E_{gap}/nKT) to measured dark currents at temperatures T > 110K. The values obtained for n range from 1.63 to 1.73. For diffusion limited dark currents n is equal to 1. With arrays produced for JWST it has been demonstrated that the dark current of MBE devices having a cut-off wavelength of λ_c~ 5.5 µm are dominated by a diffusion limited processes down to operating temperatures of 40 K. This is clearly not the case for the HAWK-I arrays, which have a cut-off wavelength of λ_c~ 2.5 µm.

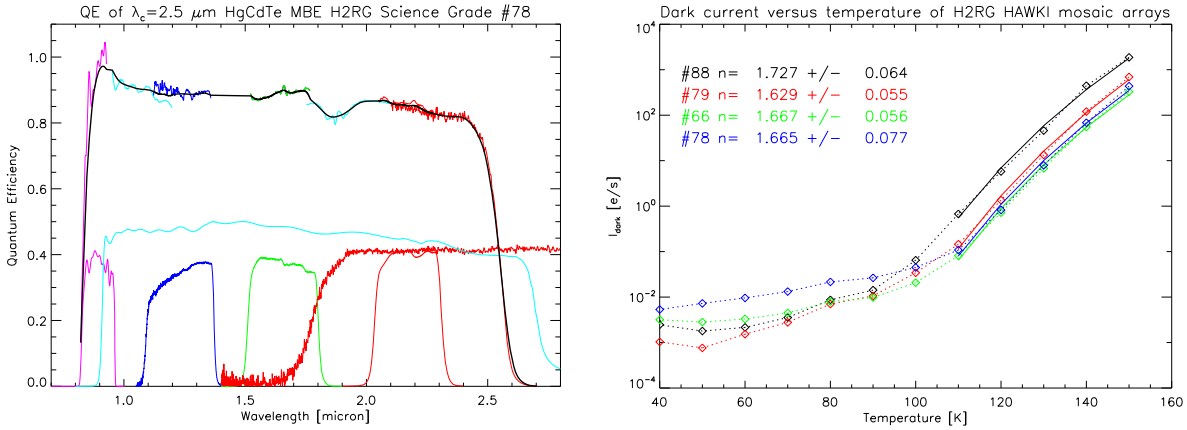

Figure 1 Left plot: Spectral quantum efficiency of λ_c~ 2.5 µm HAWAII-2RG science grade array #78. Transmission curves of used bandpass filters are indicated. Right plot: Dark current versus temperature for HAWAII-2RG arrays of Hawk-I mosaic. At operating temperatures of T>110K the dark current is proportional to exp(-E_{gap} / nK_bT) and n is obtained from a fit to measured data.

Long exposures with one of the HAWK-I arrays (device #88) are contaminated by radioactive events. On average an event hits the array every 75 seconds and the data reduction pipeline has to eliminate it by a cleaning algorithm. The radioactivity may be caused by radioactive metal sheets used in the BCS structure onto which the array is glued. The central pixel hit by an event gets a signal of > 100000 electrons which is beyond the saturation level of the detector. An event affects an area of ~ 7x7 pixels. The total integrated intensity of an event is about 740000 electrons.

3. READOUT NOISE

The readout noise of the four HAWAII2-RG arrays in the Hawk-I mosaic measured with double correlated sampling ranges from 12.6 to 16.5 electrons rms. The readout noise of these arrays is not limited by the readout multiplexer or the data acquisition chain, but by the noise of the infrared active pixels as shown by the noise map of array #88 in the left image of Figure 2. The noise map displays a section at the right edge of the array with 4 columns of reference pixels. The noise of the infrared active pixels is 16.5 erms, but the noise at the left edge in the stripe of the 4 columns of reference pixels is only 8 erms. The HAWAII-2RG arrays are surrounded by these reference pixels. In contrast to the standard infrared-active pixels, the reference pixels are not connected to IR detector photodiodes. Instead, they contain a simple capacitor C_{pix} in the Si multiplexer whose capacitance is similar to the detector capacitance. The reference pixels are used to track possible bias or temperature drifts and subtract low frequency noise pick-up. For each row the 4 reference pixels read at the beginning of the row in channel 1 and at the end of the row in channel 32 are median filtered and subtracted from the pixel values in all channels of the corresponding row. The lower noise level observed on reference pixels proves that the contribution of the readout multiplexer and the rest of the data acquisition chain to the overall readout noise is small. The cryogenic preamplifiers and the external controller electronics are no major noise drivers.

The observed readout noise is dominated by noise sources intrinsic in the infrared diode of the detector pixel, possibly the Ohmic resistance of the pad contact.

Out of the large number of arrays which have been tested at ESO two arrays have a readout noise which is a factor of two lower than that of standard arrays. The right image in Figure 2 shows the noise map of the low noise device #49 with the same scaling. For this device infrared active pixels and reference pixels both have a readout noise of 8.2 erms. Since the reference pixels of both device #88 and device #49 have the same readout noise of 8 erms, but only device # 49 has the low noise on the infrared pixels, this is further evidence that the readout noise of 15 to 20 erms measured on most HAWAII -2RG arrays is generated in the infrared active pixels. For the low noise device #49 the plot in Figure 2 shows the reduction of readout noise with the number of nondestructive readouts using Fowler sampling when the detector is continuously read out at the maximum frame rate maximizing the number of readouts for the given integration time. Hence, the detector integration time scales linearly with the number of readouts. For 64 nondestructive readouts or 32 Fowler pairs the integration time is 52.8 seconds. The lowest readout noise on the active IR pixels is 2.4 erms with 32 Fowler pairs.

This outstanding performance figure impressively demonstrates two accomplishments of the HAWAII-2RG multiplexer design. First, the shielding of the multiplexer glow, which limited the number of Fowler pairs with previous multiplexers because of glow-induced photon shot noise, has been implemented very efficiently in the HAWAII-2RG multiplexer. Second, the implementation of 32 parallel video channels not only reduces the readout time but more importantly, also improves the noise performance, since more non-destructive readouts can be made within a given integration time.

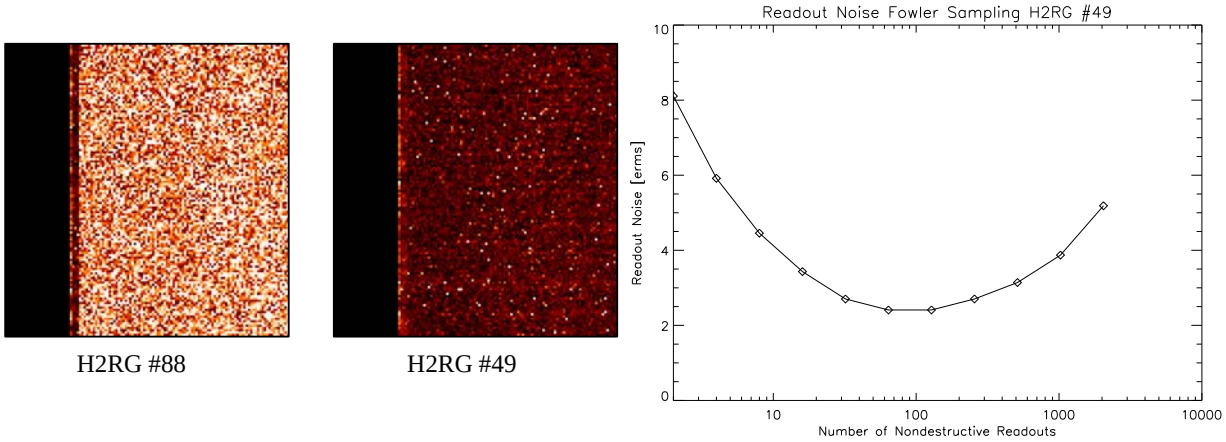

Figure 2 Left image: Noise map of HAWAII-2RG #88. Noise of reference pixels in 4 columns at the left edge: 8erms. Noise of infrared active pixels: 16.5 erms. Right image: Noise map of HAWAII-2RG #49. Noise of both reference and infrared active pixels 8 erms. Right plot: Readout noise versus number of nondestructive readouts with Fowler sampling. Readout noise 2.4 erms for 32 Fowler pairs.

4. TIP-TILT CORRECTION AND FAST PHOTOMETRY WITH THE GUIDE WINDOW

The HAWAII-2RG array has a built in guide window mode. A guide window can be read in an interleaved way with the full science frame. Since the 2x2 mosaic installed in the HAWKI camera has 4 arrays, all four 16x16 pixel guide windows are concatenated into a single 32x32 pixel frame and stored in a data cube. The guide windows are read at time intervals of 6.3 ms after every full frame row readout (2048 times per full science frame). The readout noise of the guide windows containing the empty sky is 14 erms. A bright star of m_J =5.16 was used to measure the power spectral density of the image motion. Most of the spectral power of the star position offsets is contained at frequencies below 10 Hz. A slow tip tilt correction of < 10 Hz is sufficient for the efficient correction of the image motion. The standard deviation for the star position was 0.95 pixels corresponding to 95 milliarcseconds on the sky (pixel scale of HAWK-I mosaic 0.1 arcsec/pixel).

The guide window of the HAWAII2 - RG detector was also tested with a fainter calibration star of magnitude m_J=12.48. The seeing was 0.7 arcsec. The guide window was read 128 times per full science frame at a rate of 64 Hz. Every 15.6

ms a new shift vector was calculated. The upper image at the right in Figure 3 shows the average of 5000 guide window frames. In the lower image of the same figure the frames have been re-centered before averaging. In this way guiding errors and atmospheric tip-tilt is corrected. The peak intensity in the re-centered average of the images is 118.8 ADU whereas the peak intensity of the uncorrected average is 97.4 ADU as shown by the intensity profiles in Figure 3. This re-centering corresponds to an increase of Strehl ratio of 20 %. The full-width-half-maximum of the uncorrected image is 0.82“ and the re-centered image has a FWHM of 0.72 “.

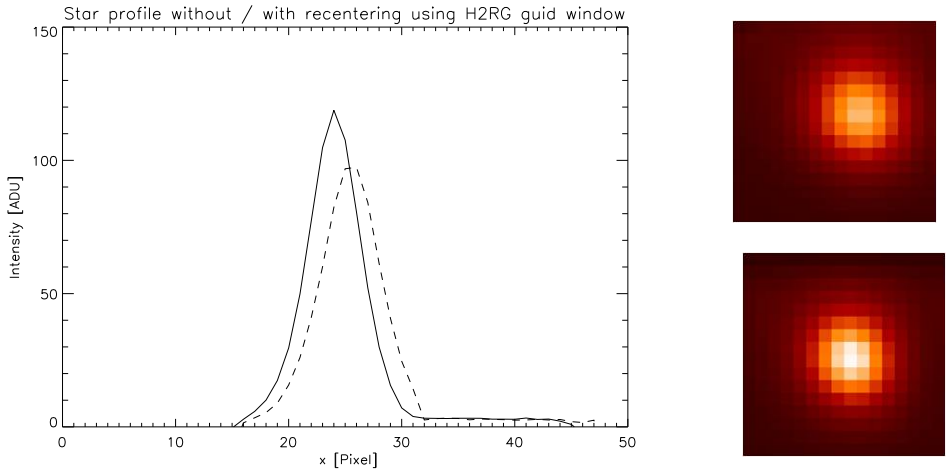

Figure 3 Profile of calibration star with re-centering (solid line and upper image) and without re-centering (dashed line, lower image).

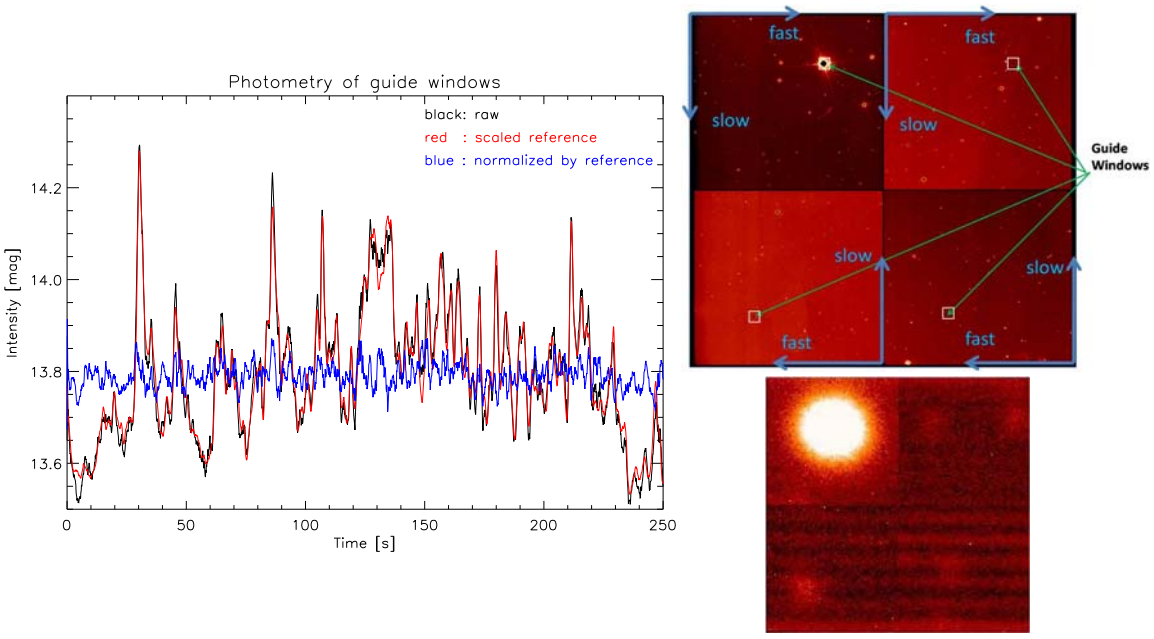

Figure 4 Fast photometry using guide windows. Four 64x64 pixel guide windows were taken in J band with integration times of 83 ms to measure isoplanaticity of image motion and correlation of photometric flux as a function of Separation. Upper right image: orientation of fast and slow shift registers on HAWKI mosaic and placement of guide windows. Lower right image: concatenation of four 128x128 pixel guide windows.

The readout of the guide window does not generate artifacts on the science frame, as can be seen in the upper right image of Figure 4. In Hawk-I the guide windows need to be placed at the same location on each detector since each detector receives exactly the same clocks and bias voltages and cannot be programmed individually. However, due to the orientation of the arrays in the mosaic (see upper right image of Figure 4) it is possible to change the separation of the guide windows and to match the distance between two objects for doing fast photometry concurrently on two regions of interest. The scintillations of a faint object of interest can be calibrated by performing photometry on a bright reference object in the field of view. Data cubes have been taken with stars in all 4 guide windows to measure the correlation of photometry as a function of distance. A short time exposure of the concatenated 4 guide windows is shown in the lower right image of Figure 4. Aperture photometry was performed on the two left ones of the four 80x80 pixel sub-windows which have been read out every 126 ms using the double correlated readout mode. The black curve in the plot of Figure 4 shows the photometry of a star of magnitude 13.8 contained in the lower left of the guide windows in Figure 4. The scintillation is 0.13 magnitudes rms. The red curve is a reference star of magnitude 9 (upper left guide window in Figure 4) scaled to the intensity of the faint star. The blue curve is the intensity of the faint star divided by the intensity of the bright reference star. After division the scintillation of the faint star is reduced to 0.026 magnitudes rms. The reference star tracks the intensity variations of the faint star. The separation of the star and the reference star was 219.7 arcsec. The guide windows open up new possibilities in fast photometry observing extra-solar planet transits and occultations.

5. ELECTRICAL GHOSTS BY INTER-CHANNEL CAPACITIVE COUPLING

If a bright point source or spectral line is imaged onto the array, shadow images can be observed on some of the other 32 video channels. The strength of the inter-channel coupling follows an irregular pattern and may be small or negligible for adjacent channels. This is particularly cumbersome in a cross-dispersed echelle spectrograph with lots of bright calibration lines or sky lines. An example of inter-channel coupling is shown in Figure 5 displaying echelle orders of a cross-dispersed echelle spectrograph and bright spectral lines with their corresponding electrical ghosts. It is difficult and cumbersome to disentangle weak spectral lines from electrical ghosts of strong atmospheric emission lines or calibration lines. The 32 video channels of the HAWAII-2RG are organized in 32 vertical stripes. For example, a bright spectral line imaged onto channel number 23 generates the strongest ghosts in channel number 21 and channel number 32. The HAWAII -2RG array was operated with the default readout directions. Odd channels are read from left to right and even channels from right to left. The trapezoids in Figure 5 indicate areas of pixels in the respective channels which are read out concurrently with the bright spectral line.

A trace through the bright spectral line in channel number 23 is shown in the left plot of Figure 6 together with the trace of the ghosts in channel number 21 and 32. The trace of the bright line was divided by 50 to scale the plot to the intensity of the ghosts which were not scaled. The ghosts show a positive and a negative shadow. Their signs are inverted because the readout direction of channel 32 is the opposite of channel number 21. The intensity of the ghosts are proportional to the slope of the spectral lines. Actually, the ghost is proportional to the differentiated signal of the spectral line as is to be expected for capacitive coupling onto a resistor in a simple RC differentiator. The peak intensity of the ghost in channel 32 is 1 % of the bright spectral line. As can be seen in Figure 5, the electric ghosts contaminate the free spectral range of a cross-dispersed instrument and present a difficult problem for the data reduction.

We checked the layout of our cryogenic preamplifier board and tested it by feeding one channel with a clock signal while observing the crosstalk to other channels; we could however not establish a correlation between crosstalk on the preamplifier board and electrical ghosts observed with the detector. Electrical ghosts were also observed at CFHT with the WIRCAM mosaic and at ESO with the HAWK-I mosaic. It is noteworthy that there is no coupling between detectors of the HAWK-I mosaic, even though all clocks and bias voltages are shared among the 4 detectors.

It is assumed that the coupling occurs either inside the HAWAII-2RG multiplexer or in the wirebond ceramic. A correlation between their layouts and the strongest capacitive coupling constants observed with the detector is still to be investigated. The only method which helps to reduce the inter-channel coupling is the reduction of the readout speed. The right plot of Figure 6 shows the integrated intensity of the ghost in channel 28 versus the pixel time with the bright source illuminating channel 16. Diamonds represent the intensity of the positive ghost and triangles the negative ghost. For larger pixel times the intensities of the ghosts decrease. The ghosts can be further reduced to a negligible level by

increasing the current through the unit cell source follower. For this purpose VBIASGATE has to be changed from the nominal value of 2.4 V to 2.0V.

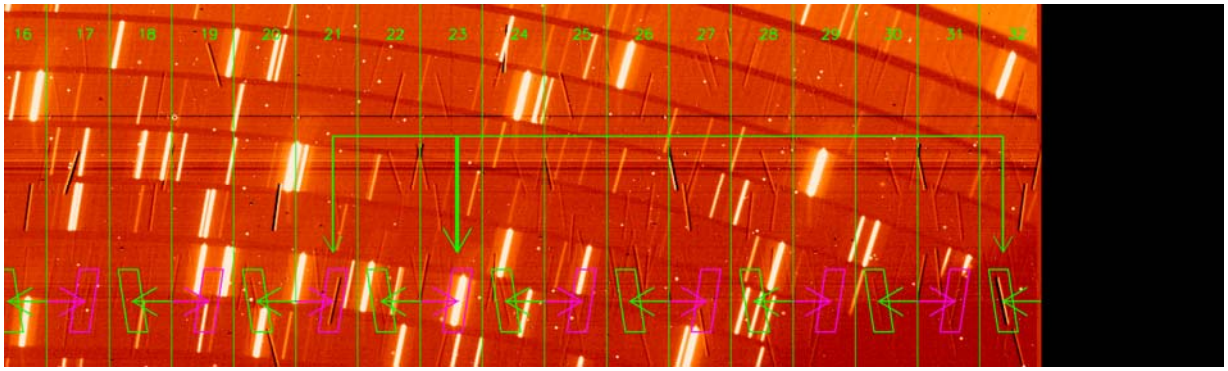

Figure 5 Electric ghosts of HAWAII-2RG in X-Shooter. Bright line in channel 23. Strongest ghosts in channel 21 and channel 32. Readout directions of odd channels: left to right, even channels right to left. Trapezoids indicate areas of pixels read out at the same time in the respective channels as area containing bright spectral line in channel 23 .

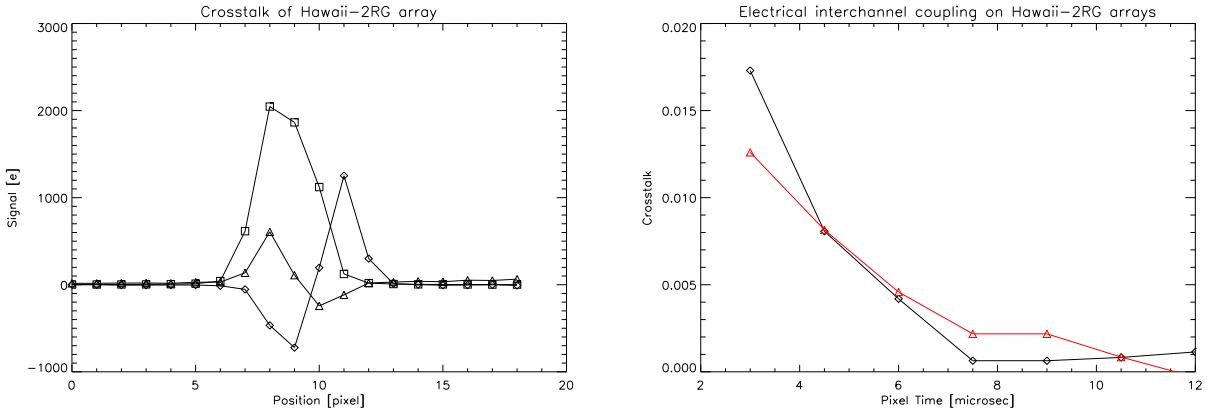

Figure 6 Left: Intensity traces of spectral line and electric ghosts on the HAWAII -2RG array. Squares: Bright spectral line in channel number 23 divided by 50. Triangles: Electric ghost in channel number 21. Diamonds: Electric ghost in channel number 32. Right: Absolute value of integrated crosstalk versus pixel time with bright source in channel 16 and ghost in channel 28. Diamonds: Positive ghost. Triangles: Negative ghost.

6. FRINGING IN THE DETECTOR SUBSTRATE

Until recently HgCdTe HAWAII -2RG detectors, which are grown on a CdZnTe substrate have been delivered with the substrate thinned to a thickness of ~ 800 μm. This substrate is a parallel plate which has a refractive index of 2.7. Even though the surface of the substrate has an anti-reflection coating, the reflectivity is not zero. Hence, the parallel plate of the substrate acts like a Fabry-Perot with multiple reflections generating interference fringes when put in the focal plane of a high resolution echelle spectrograph.

As an example, the left image of Figure 7 shows the fringing in the X-Shooter spectrograph displaying a section of the long wavelength orders of the cross dispersed echelle spectrum [3]. The upper most band in Figure 7 is order 11 of the

echelle spectrum and covers the spectral range from 2.271 μm to 2.478 μm with a spectral resolving power of R > 5000. A trace of the regularly space fringes in the center of echelle order 11 is shown in Figure 8. The spectral separation of the fringes $\Delta\lambda$ is 1.235 nm at a wavelength λ of 2380 nm. The refractive index n of CdZnTe is 2.7. With these parameters the thickness d of the substrate which is equal to $\lambda^2/(2n\Delta\lambda)$, can be calculated to be 849 μm, which is the expected value.

The fringe contrast, which is defined as the ratio of the maximum and the minimum of the transmission of a Fabry Perot is $(1+R)^2/(1-R)^2$ where R is the reflectivity. The observed fringe contrast of ~ 1.4 corresponds to a reflectivity as low as ~ 8%. The fringing is a problem for a Cassegrain instrument such as X-Shooter which has flexure. Spectra taken with different gravity loads do not subtract well because the fringes move on the detector. This presents a serious problem for flat fielding.

Fortunately, ESO had a substrate removed engineering grade array available for replacing the X-Shooter array. The right image in Figure 7 shows the same section of the spectrum and impressively demonstrates that substrate removal completely eliminates the fringing. We tried to reproduce the detector fringing in a laboratory setup with a monochromator and pen ray lamps. However, the interpretation of the fringes is difficult, since the entrance window of the cryostat, the interference filter and the detector substrate form three coupled Fabry Perots in series and each of them produces its own fringes.

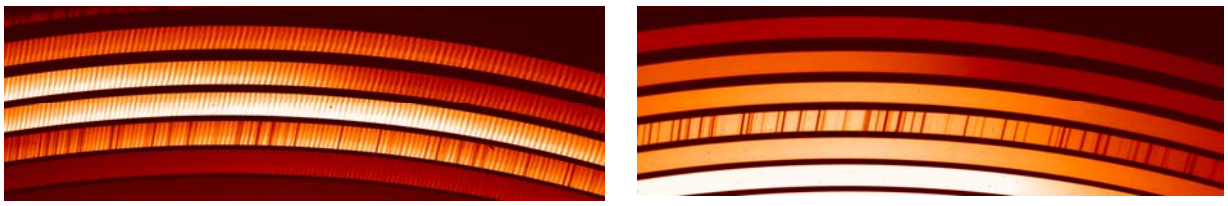

Figure 7 Left image: Detector with CdZnTe substrate shows fringing. Right image: Detector with CdZnTe substrate removed shows no fringing.

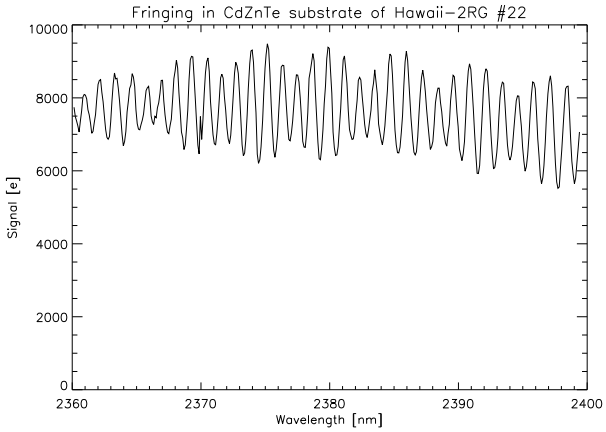

Figure 8 Fringes in CdZnTe detector substrate of HAWAII-2RG array in order 11 of cross-dispersed echelle spectrum of HAWAII-2RG array.

7. THRESHOLD LIMITED INTEGRATION "TLI"

The sample-up-the-ramp or nondestructive readout mode which is the default mode in ESO instruments, offers a simple way to expand the dynamic range of the detector for long integration times, which we call TLI (Threshold limited integration). The method only requires the definition of a threshold level in ADU units which is below the detector saturation. All pixels which have absolute ADU values below this threshold are processed normally (pixel with blue integration ramp in Figure 9). Once pixels illuminated by a bright star have absolute ADU values above the threshold these values are no longer taken into account for calculating the slope of the regression fit (pixel with red integration ramp in Figure 9). For those pixels only nondestructive readouts having values below the threshold are taken into

account to calculate the slope of the integration ramp. The pixel value written into the fits file is the value extrapolated to the total integration time. It is calculated from the slope using only non-saturated nondestructive readouts as illustrated in Figure 9.

The left image in Figure 10 shows a K-band image of a cluster without setting a threshold level. The cores of the two encircled stars are saturated in their centers. In the right image of Figure 10 the threshold for TLI was set to 30000 ADU, which is well above the average sky level. The two encircled stars are no longer saturated. Their photometric intensity ratio is 1.84. Their intensity ratio was also measured with a 5 s exposure when both stars are not saturated and TLI is not needed. The ratio measured with the 5 s exposures was 1.83. The intensity ratios of saturated long exposures with TLI and short exposures without TLI agree to within 0.67 %.

Even though readout values of brightly illuminated pixels are not used, they get physically saturated, once they come close to the saturation level. Hence, the persistence which is stronger for highly saturated pixels remains. It must also be noted, that the effective integration time for bright stars is not the total detector integration time, but only the time until the star has reached the saturation limit. Bright pixels have a shorter integration time which will reduce the signal to noise ratio. In practice this is not a problem, since the signal to noise for bright stars is high. Finally, a very bright star (of the order of < 9 mag) will saturate the pixel already during the first non-destructive readout and its intensity cannot be measured with TLI, which at least requires two nondestructive readouts below the saturation level. Since TLI preserves the accuracy of the photometry to better than 1% this mode is now routinely offered at the telescope.

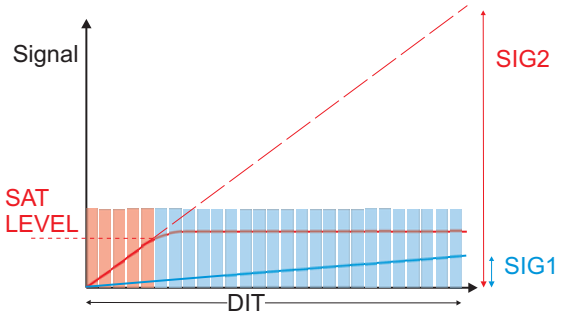

Figure 9 Saturation threshold for nondestructive sampling and extrapolation of detector signal for high flux levels. For pixels with high flux (red) only pixel values below SATLEVEL are taken into account for calculation of slope. For low flux pixels (blue) all nondestructive readouts indicated by rectangles are use. (for colors see: www.eso.org/~gfinger)

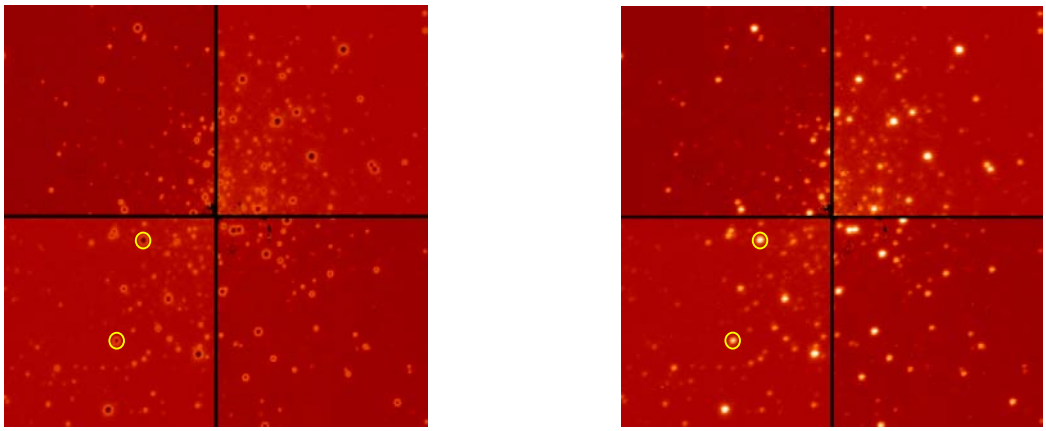

Figure 10 K-band image of cluster. Cut levels: 0 /240000 ADU.Integration time 30 s. Left: without TLI. Encircled stars are saturated. Right: With TLI activated and threshold level set to 30000 ADU. Encircled stars not saturated.

8. IRON 55 AS NEW CALIBRATOR FOR SUBSTRATE REMOVED MCT

The X-ray photons of the Fe^{55} decay are used to calibrate the conversion gain of optical Silicon detectors for both CCD's and CMOS devices. Each photon emitted in the K_α line at 5.9 KeV which is absorbed in Silicon generates 1620 electrons [4]. With HgCdTe detectors on a CdZnTe substrate it is not possible to extend this well established calibration procedure to infrared wavelengths. The reason is that the X-ray photons are absorbed in the CdZnTe substrate and do not reach the detector.

However, the new generation of HAWAII-2RG HgCdTe detectors are delivered with the detector substrate removed. Detectors are still grown on the substrate but the substrate is then removed by a first mechanical lapping and then a chemical etch. Hence, the X-ray photons which are directly absorbed in the top layers at a depth of 1-2 μm of the infrared sensitive HgCdTe detector generate electron hole pairs which are collected on the integrating node capacitance of the detector. A prerequisite to establish the Fe^{55} method to infrared wavelengths is the reliable calibration of the integrating node capacitance C_0 and the corresponding conversion gain C_0/e.

8.1 Calibration of the conversion gain with the capacitance comparison method

The conversion gain is the basic parameter on which all other detector characteristics rely. It has been shown that the usual method to determine the conversion gain from the photon transfer curve by determining the signal variance as a function of the signal and deriving the conversion gain in e/ADU from the inverse slope of this plot is only correct, if the signal of adjacent pixels is uncorrelated. If the interpixel capacitance is not negligible, the signal variance which is equal to the autocorrelation function at zero has to be replaced by the integrated autocorrelation in order to derive the correct conversion gain which properly takes the interpixel capacitance into account. An alternative and more direct method, the capacitance comparison method, has been developed which directly determines the capacitance of the detector integrating node by comparing the node capacitance with a large external, calibrated capacitor. This technique is simple to apply and does not rely on stochastic methods which also have their limitations [5,6].

The technique requires a small hardware modification to the detector control electronics; it entails adding a switch (relay) between the bias and V_{reset} and adding a calibrated capacitor, C_{ext}, between V_{reset} and detector substrate voltage D_{sub} as shown in Figure 1. The modification was implemented on the basic board of ESO's new NGC controller generating the analog clock an bias level. During normal operation the reset voltage, V_{reset}, is connected to an external bias voltage of the detector control electronics and the bias provides the charge required to reset the integrating node capacitance. The external capacitor is charged to the nominal reset voltage and disconnected (using the relay) from the external bias. The charge to reset the nodal capacitance C_0 of each pixel slowly discharges the external capacitor, C_{ext}. If the 2Kx2K pixels of the detector are exposed to a high photon flux and several frames are read out and reset, the charge to repeatedly reset the complete array will discharge $C_{ext,}$ generating a voltage drop across C_{ext} large enough to be measured accurately. In our setup the capacitance of the cables interfacing the control electronics to the detector, the filter capacitors on the cold detector board inside the cryostat and the filter capacitors on the wirebond ceramic with the PGA connector on the backside of the detector are all parallel to the large calibrated external capacitance C_{ext}. They are summarized in a cryo capacitance C_{cryo}.

$$\Delta V_{ext}(C_{ext} + C_{cryo}) = \sum_{n=1}^{n_{frames}} \sum_{i=1}^{2048} \sum_{j=1}^{2048} V_{n,i,j} C_0$$

$$\alpha = \frac{\Delta V_{ext}}{\sum_{n=1}^{n_{frames}} \sum_{i=1}^{2048} \sum_{j=1}^{2048} V_{n,i,j}} = \frac{C_0}{(C_{ext} + C_{cryo})} \qquad (1)$$

Since the voltage drop ΔV_{ext} on C_{ext} and the signals of each pixel $V_{i,j}$ are known, the nodal capacitance C_0 and thus the conversion gain C_0/e can be calculated as shown in Eq. (1).The detector signal $V_{i,j}$ and its change in DC level ΔV_{ext} can be observed by using the normal data acquisition chain operating the detector in the read-reset-read mode. By simply recording the raw data values before and after reset rather than the differences, as would normally be done in double correlated sampling, both the pixel intensities and the DC level of the detector signal can be calculated.

Depending on the photon flux to which the detector is exposed, the DC level of the detector signal drops at a proportional rate ΔV_{ext} /frame in ADU's per frame. The number of frames can be selected to be sufficiently large to measure the voltage drop per frame ΔV_{ext} with the desired accuracy.

For the measurement the first substrate removed λ_c~ 2.5 µm engineering grade HgCdTe array delivered to ESO was used. The voltage drop ΔV_{ext} is measured at different photon flux levels and plotted in Figure 5 versus the sum of the detector signal for the corresponding flux level. Since any leakage current of the external capacitances and cables does not change with varying photon flux level, the slope α of the dc level drift over the total detector signal does not depend on the leakage current.

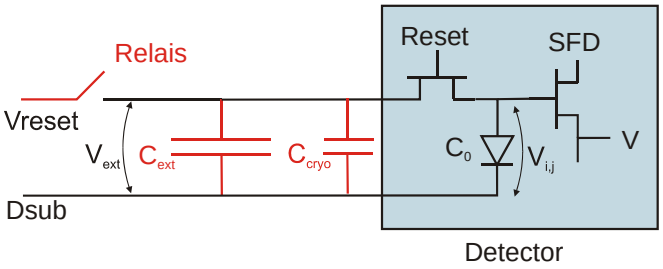

Figure 11 Hardware setup for capacitance comparison method for the measurement of the conversion gain.

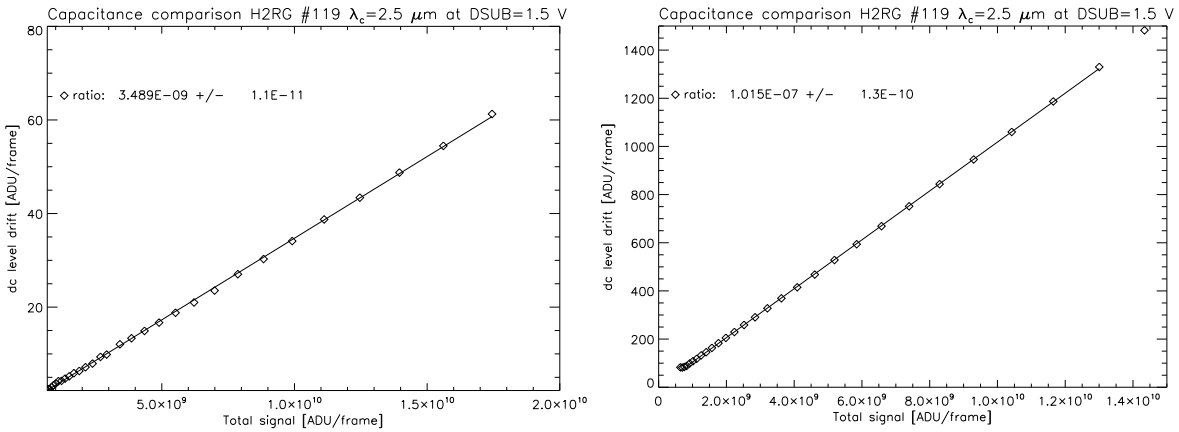

Figure 12 Voltage drop across the external capacitance V_{ext} versus the sum of the voltages of all detector pixels (total detector signal) for the corresponding flux level. The total detector signal is changed by increasing the photon flux on the detector. The slope α of the least square fit is the ratio of the nodal capacitance and the external capacitance $C_0/(C_{ext}+C_{cryo})$. Left plot: External capacitance C_0 connected. Slope α=3.489E-9. Right plot: External capacitance C_0 removed. Slope α_0=1.015E-7.

The capacitance C_{cryo} of the cold filters inside the cryostat is difficult to measure without putting the detector at risk. Even if the capacitances are measured at room temperature, the capacitances of ceramic capacitors may change substantially. For example the 1 µF ceramic capacitors used on the HAWAII-2RG wirebond ceramic were measured to drop to 276nF at liquid nitrogen temperature.

However, C_{cryo} can also be retrieved from the measured slopes α and α_0 of Figure 12. α is the slope measured with the external capacitor C_{ext} connected and slope α_0 is measured with the external capacitance C_{ext} removed (C_{ext}=0). In this case only the cold capacitance C_{cryo} inside the cryostat remains connected and C_{cryo} is $C_{ext}\alpha/(\alpha_0-\alpha)$. The node capacitance C_0 can be determined from the slope α by introducing an additional correction factor $1/(1-\alpha/\alpha_0)$ which

accounts for the off chip capacitance on the detector board inside the cryostat and the cable capacitance. The formulas for C_0 and C_{cryo} are shown in equation (2)

$$C_0 = C_{ext}\frac{\alpha}{1-\frac{\alpha}{\alpha_0}} \qquad C_{cryo} = C_{ext}\frac{\alpha}{\alpha_0 - \alpha} \tag{2}$$

The external capacitance C_{ext} used in our setup was 9.83 µF. It was calibrated by the EADS calibration service. With the slope measurements of Figure 12 and equation 2 we get C_{cryo} = 350 nF including the capacitances of the cables, the capacitances on the preamplifier board and on the wirebond ceramics. The estimated value for C_{cryo} is ~ 310nF which is in good agreement with the measured value considering the uncertainties of the estimation. With these values the nodal capacitance C_0 of the detector is 35.5 fF and the conversion gain C_0/e is 222 e/mV. In our setup this corresponds to 2.12 electrons per ADU.

8.2 Extension of the Fe55 method to λ_c ~ 2.5 µm HgCdTe

Having calibrated the conversion gain of the substrate removed HgCdTe detector by the capacitance comparison method it is now possible to measure the number of electrons generated by the absorption of K_α photons of Fe^{55} by counting the total number of ADU's per event. For this purpose a radioactive probe was mounted in the dark position of the cold filter wheel directly in front of the detector of our test cryostat. It is necessary to cool the radioactive probe to cryogenic temperatures in order to perform the measurement under low background conditions. The activity of the Fe^{55} source is 200 KBq. The source is a gold plated 200 µm thick stainless steel disk of 4.65 mm diameter which is Fe55 plated and Nickel coated to provide protection against radioactive contamination. The source is mounted in a cylindrical capsule of 8mm x 5mm and can easily be put in a free position of the filter wheel. Repeated cooldown cycles did not cause any problems of contamination. The filter wheel allows switching between dark positions with and without the Fe^{55} source.

To reduce the number of pixels which are hit by two X-ray photons the detector integration time is shortened to 427 ms by reading out only a stripe of 256x2058 pixels. For the determination of the histogram differences of dark exposures with and without the Fe^{55} probe were used. A find algorithm located the X-ray hits on the array and aperture photometry was applied to each event with an aperture radius of two pixels. The residual background of the difference image was subtracted using the average in an annulus with an inner radius of 3 and an outer radius of 5 pixels. The histogram of the K_α line is shown in Figure 13. Each absorbed photon generates 2491 electrons. The small peak at 5000 electrons is due to pixels which have been hit by two photons.

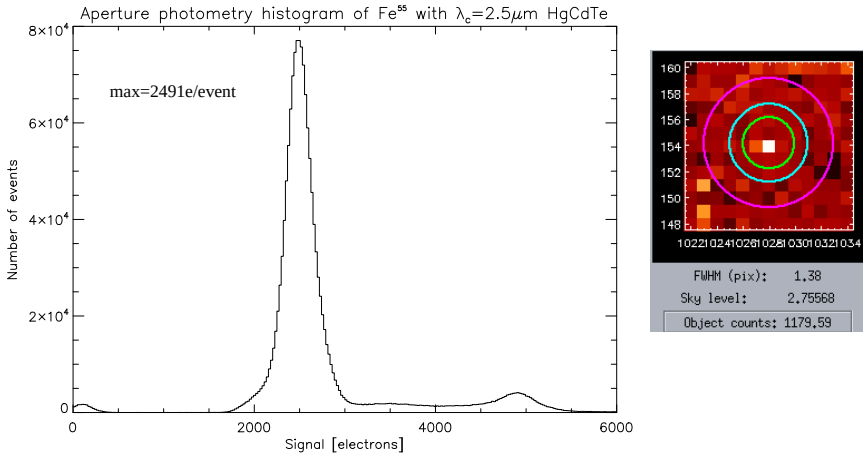

Figure 13 Histogram of the K_α line of Fe^{55} generated with aperture photometry. Each event generates 2491 electrons.

The histogram in Figure 13 does not resolve the K_α and K_β lines. Even if only the 4 next neighbours of the pixels hit by an X-ray photon are added the lines cannot be resolved. Only raw histograms resolve the lines as shown in Figure 14 by the dashed line. The absorption of a K_β photon having an energy of 6.49 KeV generates 2744 electrons which is consistent with the 2491 electrons generated by K_α photons at 5.9KeV. The intensity ratio K_β to K_α in Figure 14 is 8 to 1 whereas the ratio observed in Silicon is reported to be 7 to 1 [4].

Even those pixels which absorb photons in their center with negligible charge diffusion to neighbours generate a signal on adjacent pixels because of coupling by interpixel capacitance [6]. A correction factor of 1.129 has to be applied to values on the abscissa of the raw histogram in Figure 14 to account for capacitive coupling between neigbouring pixels. The correction factor places the peak of the raw histogram to the position obtained with aperture photometry and is shown by the solid red line in Figure 14. Using the free particle approximation a semi-empirical linear relation between the energy ε required for the creation of an electron-hole pair and the band gap energy E_{gap} was published by Bloomet al. [7]. It is shown in equation (3):

$$\varepsilon = 2.73E_{gap} + 0.55eV \tag{3}$$

The measured electron-hole pair creation energy is plotted on the right of Figure 14 for different semiconductors as function of their band gap energy. The straight line is the fit given in equation (3) to experimental data. The value obtained above for λ_c~ 2.5 µm HgCdTe is plotted as red circle. The measured pair creation energy of 2.364 eV is too high for the λ_c~ 2.5 µm substrate removed HgCdTe material which has a band gap energy of 0.496 eV. Equation (3) predicts a creation energy of 1.904 eV. The X-rays are absorbed in the first 1-2 microns of the back side illuminated detector. The λ_c~ 2.5 µm detector may be graded and have top layers of shorter cutoff wavelengths. To fit on the straight line of equation (3) the surface layer should have a cutoff wavelength of λ_c~ 1.867 µm. Fox et al. have applied the Fe^{55} X-ray technique to λ_c~ 1.7 µm HgCdTe HAWAII-2RG arrays using completely different methods of calibration and obtain 1849 electrons per absorbed K_α photon [8]. This corresponds to a pair production energy of 3.21 eV which is also higher than predicted by equation 3. Their measurement, which is consistent with our data for λ_c~ 2.5 µm material, is also included in the right plot of Figure 14 as a green cross.

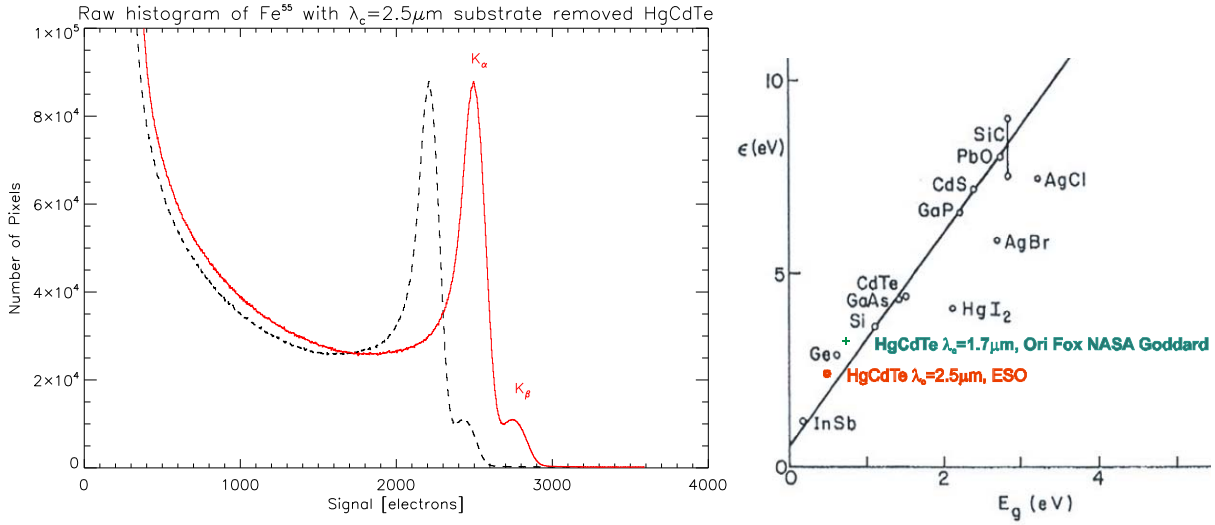

Figure 14 Left: Dashed line: Raw histogram of Fe55 decay. Solid line: Modified histogram with number of electrons multiplied by factor 1.129 setting the peak of K_α line to same position as determined with aperture photometry in Figure 13. The correction factor takes into account the effect of the interpixel capacitance.
Right: Measured electron-hole pair creation energy versus band gap energy for different semiconductors and straight line fit as given by equation (3). The value obtained here for λ_c~2.5 µm HgCdTe is shown as red circle, the value for λ_c~1.7 µm HgCdTe as a green cross[8]. (for colors see: www.eso.org/~gfinger)

The applicability of the Fe55 method as a new standard for measuring the conversion gain depends on the variability of the cutoff wavelength of the surface layers of the detector material. More samples of $\lambda_c \sim 2.5$ μm arrays have to be measured.

9. CONCLUSIONS

Because of their excellent performance characteristics the 2Kx2K HgCdTe HAWAII-2RG arrays have become the workhorses of near infrared astronomy. They have quantum efficiencies exceeding 85%. The typical DCS readout noise of ~ 15 erms mainly originates in the infrared active pixels. For selected arrays the readout noise is as low as 8.2 erms which is the value also measured on reference pixels. The readout noise can be reduced to 2.4 erms by multiple sampling. The guide window of the HAWAII-2RG array is a powerful tool for fast photometry. Inter-channel crosstalk of the HAWAII-2RG array produces electrical ghosts which can be reduced by slowing down the readout speed. In high resolution spectrographs fringing in the detector substrate is a serious problem, which fortunately is eliminated with the advent of substrate removed arrays. Threshold limited integration was implemented to extend the dynamic range of the detector. The capacitance comparison method was refined and includes now a correction for the cable capacitance and all cold capacitors near the focal plane. The method was employed to calibrate the number of electrons generated in a substrate removed λ_c=2.5 μm HgCdTe array. The absorption of a K_α photon emitted by an Fe^{55} source generates 2491 electrons. The K_α and K_β lines could be well resolved. Fe^{55} may become a new calibrator for the determination of the conversion gain of infrared arrays.

REFERENCES

[1] Moorwood A., “Instrumentation at the ESO VLT”, Proc. SPIE 5492, 626904, (2006).

[2] Kissler-Patig M., Pirard, M. Casali J.-F., Moorwood, A., Ageorges N., Alves De Oliveira C., Baksai P., Bedin L., Bendek E., Biereichel P., Delabre B., Dorn R., Esteves R., Finger G., Gojak D., Huster G., Jung Y., Kiekebush M., Klein B., Koch F., Lizon J.-L., Mehrgan L., Petr-Gotzens M., Pritchard J., Selman F. and Stegmeier J., “HAWK-I: The High-Acuity Wide-field K-band Imager for the ESO Very Large Telescope”, Astronomy & Astrophysics, to be published (2008).

[3] Navarro R., Elswijk E., Tromp N., ter Horst R. , Vernet J., Finger G., Groot P., Horrobin M., Kaper L., “X-shooter Near-IR Spectrograph Arm Realisation”, Proc. SPIE 7014, to be published, (2008).

[4] Janesik J. R., “Scientific Charge-Coupled Devices”, SPIE Press, p. 134, (2001).

[5] Finger G., Beletic J., Dorn R., Mehrgan L., Meyer M., Moorwood A., Stegmeier J., “Conversion gain and interpixel capacitance of CMOS hybrid focal plane arrays”, Scientific Detectors for Astronomy 2005, pp. 477-490, (2005).

[6] Finger G., Dorn R., Meyer M., Mehrgan L., Moorwood A.F.M., and Stegmeier J., “Interpixel capacitance in large format CMOS hybrid arrays”, Proc. SPIE Vol. 6276, 62760F (2006).

[7] Alig R.C. and Bloom S.,”Electron-Hole-Pair Creation Energies in Semiconductors”, Phys. Rev. Lett. 35, 1522-1525, (1975).

[8] O. Fox, “Correlated noise and conversion gain in JWST Hawaii-2RG detector arrays”, Proc. SPIE 7021, to be published, (2008).